Egypt. J. Chem. **Vol. 66**, No. 10 pp. 23 - 33 (2023)

Egyptian Journal of Chemistry

http://ejchem.journals.ekb.eg/

Synthesis and Characterization of Nonstoichiometric Cobalt/ CNTs Nano Composites for Multifunctional Applications

Ebtesam E. Ateiaa*, Abdulalah AL-Hamzia,b, M. Morsyc.d, S. Abd-Elwahab, B. Husseina*

[a]*Physics Department, Faculty of Science, Cairo University, Giza, Egypt*

[b]*Physics Department, Faculty of Education at Al-Mahweet, Sana'a University, Al-Mahweet Yemen*

[c]*Building Physics and Environment Institute, Housing& Building National Research Center (HBRC), Dokki, Cairo, Egypt*

[d]*Nanotechnology Research Centre (NTRC), The British University in Egypt (BUE), Suez Desert Road, El-Sherouk City, Cairo, 11837, Egypt*

Abstract

The present work aims to synthesize 70% cobalt / 30% multiwalled carbon nanotube (MWCNT) nanocomposites with enhanced physical properties. The structural and magnetic properties of the $Co_{1.5}Fe_{1.5}O_4$ /MWCNTs are reported. Structural, morphological properties of the nano composites are characterized by XRD, HR-TEM, Raman, and XPS techniques. XRD and HR-TEM investigations support the development of a single-phase cubic spinel structure of $Co_{1.5}Fe_{1.5}O_4$ confined on the exterior surfaces of MWCNTs. The measurements using a vibrating sample magnetometer (VSM) revealed ferrimagnetic nanocomposites. Heavy metal intrusion into the water system is a global environmental problem. Using $Co_{1.5}Fe_{1.5}O_4$ /MWCNT nanocomposites, the current study seeks to eliminate trace elements, including copper (Cu) and zinc (Zn). The main advantages of the synthesized samples include their high ad-sorption, amazing recycling efficiency, low cost, and simplicity of separation. Finally, one can conclude that the CNTs/ $Co_{1.5}Fe_{1.5}O_4$ is superior to other ad-sorbents in terms of effectiveness, sustainability, and environmental impact.

Keywords: CNTs; Cobalt nanoparticles; waste water; citrate auto combustion; magnetic parameters.

1. Introduction

Because of their high magnetic permeability and electrical resistivity, spinel ferrite nanoparticles (SFNPs) are important in many high-frequency power electronics and magnetic applications. The structure of SFNPs may support a wide range of cations in a variety of oxidation states. Their magnetic and electrical properties are heavily influenced by the concentration of ferrous and ferric ions and how they are distributed across the tetrahedral (A) and octahedral (B) sublattices [1]. The properties of ferrite materials can be enhanced by the substitution of various cations at both locations. According to this cation distribution, three types of spinel ferrites are present: normal spinel (NS), inverse spinel (IS) and random spinel (RS) ferrites. The NS and IS structures are (A)[B]2O4 and (B) [AB]O4, respectively, where A/B are di-valent / tri-valent cations and ( )/[ ] are A/B sites.

In IS, ½ of the B sites are occupied by the di-valent cations While in RF, the distribution of A and B cations in the A and B sites is random. Depending on the value of δ, $Co_5Fe_{3-5}O_4$ spinel ferrites exhibit a change in structure from NS to RS to IS.

In various spinel systems, the structural and magnetic properties can be altered by changing the composition of transition metals, crystallo-graphic coordination and charge/spin states. There is a charge

*Corresponding author e-mail: drebtesam2000@yahoo.com; (E.E. Ateia).
EJCHEM use only: Received date 11 January 2023; revised date 30 January 2023; accepted date 14 February 2023
DOI: 10.21608/EJCHEM.2023.186672.7442

transfer between metals and ligands [2,3], as well as a high-spin (HS) -low-spin (LS) transition of transition metals (TMs) under external disturbance, and chemical pressure [4]. TMs exist in several oxidations (charge) states, which display various magnetic moments depending on whether it is a "HS", "IS" or "LS" state. The TM ion's spin state depends on the crystallo-graphic configurations (A / B) that the metal occupies. For example, Co3+ in octahedral sites is predicted to prefer a "LS" state, but it is prohibited in many cases, causing unexpected magnetic behaviour to occur [5]. Therefore, it is highly promising to design materials (like Co□Fe3−□O4) that consist of TMs with appropriate magnetic properties like strong magnetization (Ms), coercivity (Hc), etc. controlled by the synthesis route, value of □ and particle size, etc. [6, 8]. The ferrites exhibit a variety of magnetic properties [9] and are ideally suited for numerous applications, including humidity sensors, and switches, magnetically guided drug delivery, etc. [10-11].

Carbon nanotubes (CNTs) have received a lot of attention in the realms of preparation and technological applications ever since Iijima's discovery of them [12]. They have also been utilized as an ad-sorbent to remove organic and/or inorganic pollutants from the environment [13]. CNTs are well known due to their exceptional qualities. It can be represented as a hollow cylinder carbon atom. It possesses tubular nanostructures with un-matched physical properties. CNTs' physical and chemical properties can be enhanced by adding metals, metal oxides, complex metal oxides, and polymers to them. CNTs are a promising material with several applications. It has become one of the headlines of nano-technology due to its attractive properties such as un-usual mechanical and electrical properties, large thermal and chemical stability, a unique hollow tubular framework, and a large aspect ratio [14]. The outstanding, and exceptional properties of CNTs make them potentially valuable in numerous applications, like polymer reinforcements [15], sensors [16], hydrogen storage materials [17], water treatment [18], optics [19] and catalysis [20]. Depending on the number of concentric graphene cylinders that tube includes, CNTs are formed in two primary forms: single-wall (SW) CNTs and multiwall (MW) CNTs, as illustrated in Fig. (2: c) [21].

Due to their remarkable electromagnetic properties and possible use in magnetic data storage devices, researchers have expressed interest in CNT-based magnetic nanocomposites and multifunctional nanocomposites [19], microwave ab-sorbing materials [21-20], magnetic force microscopes [22], and optical transducers for wearable electronics [23], etc.

To improve access to, inexpensive materials for a variety of future uses, the Co1.5Fe1.5O4 and CNT nano-composite was prepared. In this research, we have investigated the CNTs-Co1.5Fe1.5O4 composites' physical characteristics and their potential as a working material for the treatment of waste water.

2. Experimental Work

2.1. Materials

Fe $(NO_3)_3$•$9H_2O$, Co $(NO_3)2$•$6H_2O$, and citric acid with high purity (99.999%, Fisher Chemicals) were employed as starting reagents. All of the chemicals employed in the synthesis were assessed analytically.

2.2. Preparation of Spinel Ferrite Structure

The non-stoichiometric $Co_{1.5}Fe_{1.5}O_4$ NPs were synthesized by the citrate auto combustion technique using metal nitrates and citric acid as starting reactants [24]. The utilized metal nitrates have a high purity (99.99 %) were purchased from ACROS. Stirring and heating were used during the preparation technique, as shown in Fig. (1), until the desired sample was obtained.

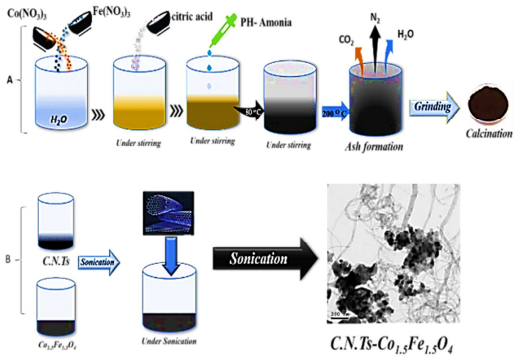

Figure (1): Schematic representation for preparation of (a) $Co_{1.5}Fe_{1.5}O_4$ nanoparticles and (b) CNTs/ $Co_{1.5}Fe_{1.5}O_4$ nanocomposites

2.3. Preparation of CNTs/ $Co_{1.5}Fe_{1.5}O_4$ Composite

Experiments on CNT growth was carried out at atmospheric pressure. As carbon sources and transport gases, acetylene and nitrogen gases were utilized. The impurities were eliminated from the CNTs by washing, and then they were dried at 60 oC. After that, MWCNTs of 30 wt.% and 70 wt.% of $Co_{1.5}Fe_{1.5}O_4$ were mixed as illustrated in Fig. (1). The resultant powdered MWCNTs were added with $Co_{1.5}Fe_{1.5}O_4$.

2.4. Characterization Techniques

XRD analyses: The crystal structure was confirmed by the X-ray diffraction (XRD) pattern of the Diano Corporation target Cu-K (λ = 1.5418 Å). The Williamson-Hall equation [25] was utilized to estimate the crystallite size of the synthesized nanoparticles. The morphology and nanostructure: The morphology and nanostructure of the sample were scrutinized by high-resolution transmission electron microscopy (HR-TEM) utilizing the Tecnai G20, Super Twin, Double Tilt model. and field emission scanning electron microscopy (FE-SEM) directed to an energy dispersive X-ray analysis (EDAX) unit to confirm the elemental structure of the prepared samples using SEM Model Quanta 250 FEG. Raman scattering (RS) is a fundamental technique for studying the essential properties of prepared samples (Horiba LabRam HR Evolution, Horiba, Ltd, UK).

The sample's X-ray photoelectron spectra (XPS) were recorded using K-ALPHA (Thermal Fisher Scientific, USA) with monochromatic X-ray Al K-alpha radiation.

Magnetic Measurements: The magnetic features of the studied nanocomposites were investigated using the VSM Model Lake Shore 7410.

2.5. Heavy Metal Removal Experiment

Heavy metals (HMs) removal from an aqueous solution for numerous elements such as Cu2+ and Zn2+ was performed in batch experiments using non-stoichiometric $Co_{1.5}Fe_{1.5}O_4$and the composite CNT-$Co_{1.5}Fe_{1.5}O_4$ as adsorbents. To study the optimum pH values of metal (Cu^{2+}, Zn^{2+}) removal, the experiments were carried out in a series of 250-mL flasks containing 0.1 g/L of $Co_{1.5}Fe_{1.5}O_4$/CNT nanocomposites powder in 2 ppm of metal nitrate. Metal ions are adjusted at various pH values from 2 to 8. The initial pH of the solution was adjusted with NaOH. The prepared solutions were dispersed well using an electric shaker (Orbital Shaker SO1) at 250 rpm for 60 min. The supernatant solutions were then collected and filtered. The concentration of metals in the filtrate was measured using inductively coupled plasma (ICP) spectrometry.

The removal efficiency and sorption capacity were determined from the following formulas [26]:

$$removal\ efficiency\ \% = \frac{C_o - C_f}{C_o} \times 100 \qquad (1)$$

$$sorption\ capacity = \frac{C_o - C_e}{m} \times V \qquad (2)$$

where Co and Cf are the initial and final concentrations (mg/L) of metal ion solution, respectively. V is the volume of the aqueous phase (L), and m (g) is the ad-sorbent's weight.

3. Results and Discussion

3.1. Structural Analyses

3.1.1. XRD Analysis

The crystallographic structure and phase composition of non-stoichiometric $Co_{1.5}Fe_{1.5}O_4$ and $Co_{1.5}Fe_{1.5}O_4$ /CNTs nano-composites are analyzed by XRD as shown in Fig. (2: a). The existence of the intended phases without the detection of any impurity is evident from the figure. The observed pattern with the (220), (311), (222), (400), (422), (511), and (440) crystal planes emphasize the formation of a cubic structure with space group Fd-3m for the investigated sample as matched with ICDD no. 01-083-3117 [27].

As depicted in Fig. (2: b), the distinctive CNT peaks can be seen at 26.5 and 43.4 degrees However, CNTs cannot be accurately portrayed by XRD [29]. This is explained by the thinness of the CNT wall [30] and the decoration of ferrites NPs on the surface of CNTs, as seen later in HRTEM images. The experimental and theoretical lattice parameters (a) [31], unit cell volume (V), theoretical density (Dx) [32], tolerance factor (T) [33], and oxygen parameters (u) [34] are calculated and listed in Table (1).

According to the pervious study, the Williamson-Hall equation [25] will be used to compute the precise crystalline size, and the results are shown in the Table. The CNTs- $Co_{1.5}Fe_{1.5}O_4$ sample shows a slight increase in the crystallite size compared to the non-stoichiometric $Co_{1.5}Fe_{1.5}O_4$ sample.

3.1.2 Raman Spectrum Analysis (RSA)

Figure (3: a-b) shows the RS for pure $Co_{1.5}Fe_{1.5}O_4$ and $Co_{1.5}Fe_{1.5}O_4$/CNTs. All peaks are present in the RS demonstrating the successful preparation of the $Co_{1.5}Fe_{1.5}O_4$/CNT composite. The five Raman active modes (A_{1g}, $1E_g$, $3T_{2g}$) are observed in the figure and match well with those of E. Ateia et al. [24]. The G band and the D band, as shown in Fig. (3: b) are the two primary Raman modes that may be seen in the spectra of MW-CNTs. The G-band, which is typically used to detect CNTs, is produced by phonon scattering at the Brillouin zone's K point.

Table 1

The experimental (aexp) and theoretical lattice parameters (atheo.), unit cell volume (V), theoretical density (Dx) tolerance factor (T), crystallite size (LW-H) and oxygen parameter (u)

Samples	a_{exp} (Å)	a_{the} (Å)	V (Å^3)	D_x (gm/cm^3)	T	L_{W-H} (nm)	u (Å)
$Co_{1.5}Fe_{1.5}O_4$	8.366	8.435	585.54	5.367	1.01	23.00	0.381
CNTs-$Co_{1.5}Fe_{1.5}O_4$	8.366	8.350	585.54	5.367	0.99	26.00	0.378

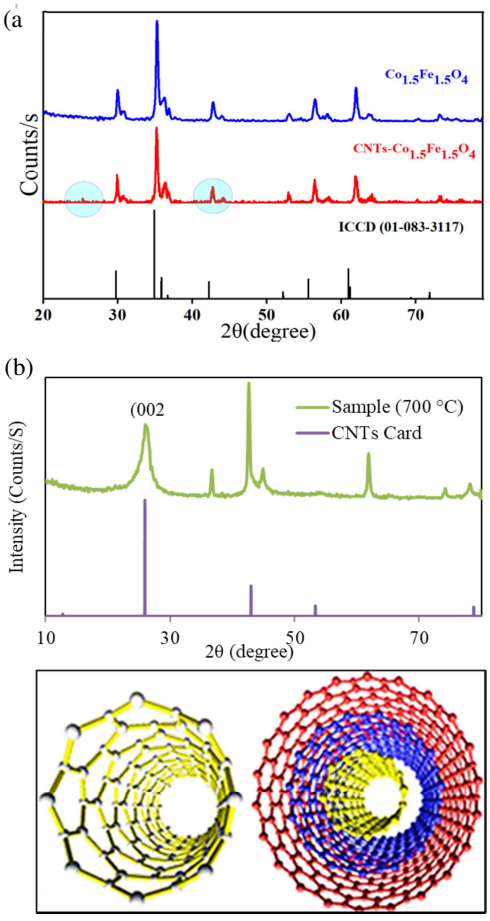

Figure (2: a-c): XRD diffraction pattern for (a) nonstoichiometric $Co_{1.5}Fe_{1.5}O_4$ and nanocomposite CNTs-$Co_{1.5}Fe_{1.5}O_4$ (b) pure CNTs (c) schematic representation for the single wall and multiwall CNTs.

This bond typically corresponds to intensification in defect density. The G band's intensity is related to the sample's crystallinity and can be used to determine the degree of CNT crystallinity [35].

In the case study, carbon materials with high levels of symmetry and ordered structure form graphitic bands (G-bands) with wavelengths ranging from 1550 to 1600 cm^{-1}. The second peak, a large D-band peak, lies in the 1385–1399 cm^{-1} range. The D-peak reveals the existence of sp2 bond breaks and carbon-like impurities in sp3 bonding, both of which cause defects in graphitic materials. On the other hand, the G band is connected to the stretching mode of sp2 bound carbon [36]. The ID/IG band ratio is the key indicator of pervasive faults in CNT architectures [37].

3.1.3. HR-TEM Analysis

As demonstrated in Fig. (4: e, f), HR-TEM imaging has recently been used to measure the tubules size and the degree of purity within the samples. The CNTs are found to be not homogeneously distributed under the synthesis conditions and nearly coated with $Co_{1.5}Fe_{1.5}O_4$. Consequently, both the isolated and the nonhomogeneous coating of $Co_{1.5}Fe_{1.5}O_4$ NPs are present.

Figure (4: c, d) represents the HR-TEM images and their selected area electron diffraction (SAED) of $Co_{1.5}Fe_{1.5}O_4$ and CNTs/$Co_{1.5}Fe_{1.5}O_4$ samples. Due to their magnetic behavior, the $Co_{1.5}Fe_{1.5}O_4$ NPs are found to be highly concentrated and to have a

propensity to aggregate. The hexagonal structure appears in images due to a slight distortion from the cubic structure into a rhombohedral one, which is confirmed by the value of the tolerance factor.

The polycrystalline structure of the $Co_{1.5}Fe_{1.5}O_4$ nano-composite is revealed by the SAED pattern. All of the diffraction rings can be correlated to cubic spinel structures (220), (311), (222), (400), (422), (511) and (440), which is in agreement with the XRD data.

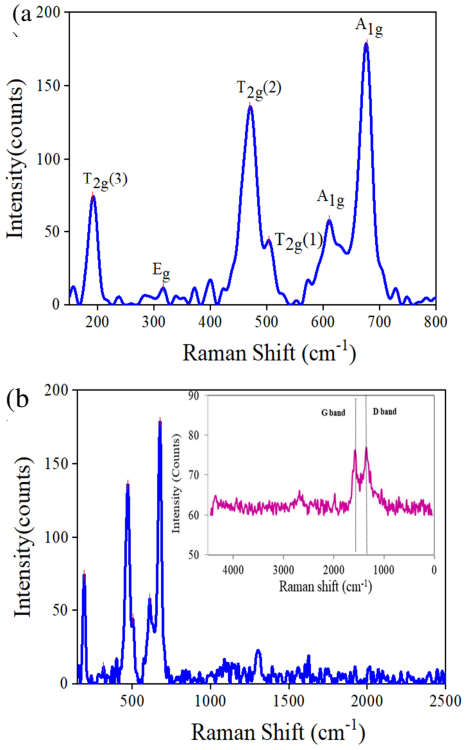

Figure (3: a, b): Raman Spectra for $Co_{1.5}Fe_{1.5}O_4$ and CNTs-$Co_{1.5}Fe_{1.5}O_4$ nanocomposite. The inset shows RS for CNT

3.1.4. FE-SEM Analysis

The morphologies of $Co_{1.5}Fe_{1.5}O_4$ and $Co_{1.5}Fe_{1.5}O_4$ / CNT nanocomposite are examined using FESEM as represented in Fig. (5: a, b). As shown in Fig. (5: a), the $Co_{1.5}Fe_{1.5}O_4$ exhibits a roughly regular grain shape with high agglomeration. Figure (5: b) depicts CNTs anchored on the surface of nonstoichiometric $Co_{1.5}Fe_{1.5}O_4$ NPs and rounded along their edges to form $Co_{1.5}Fe_{1.5}O_4$ /CNT NPs. The $Co_{1.5}Fe_{1.5}O_4$ /CNTs have less aggregation with a porous surface, as detected from the figure.

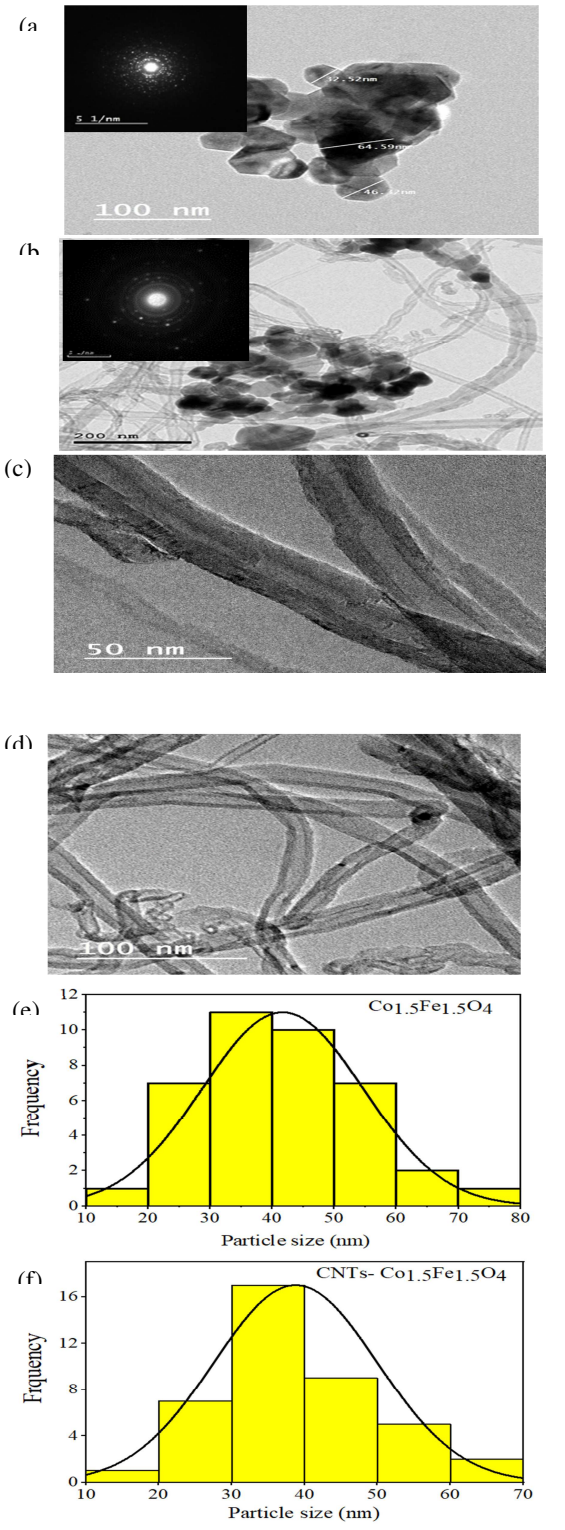

Figure (4: a-f): (a) and (b) HRTEM and SAED for $Co_{1.5}Fe_{1.5}O_4$ & CNTs-$Co_{1.5}Fe_{1.5}O_4$ nanocomposite, (c,d) represents the HR-TEM for CNTs. Fig. (e, f) the particle size distribution for $Co_{1.5}Fe_{1.5}O_4$ & CNTs/$Co_{1.5}Fe_{1.5}O_4$ NPs

3.1.5 EDAX Analysis

The chemical composition of samples under investigation is examined with EDAX. Figure (6: a-b) ratifies the existence of numerous elements (Fe, Co, and O) in the non-stoichiometric $Co_{1.5}Fe_{1.5}O_4$ NPs. However, the $Co_{1.5}Fe_{1.5}O_4$ /CNT, EDAX spectra reveal the presence of extra peaks that correspond to carbon, which originated due to the existence of MW-CNTs, as illustrated in Fig. (6: b). The examined composition agrees well with the chemical stoichiometry of the starting powders. The atomic ratios of Fe/Co were found to be 1.5:1.5 by EDAX analyses.

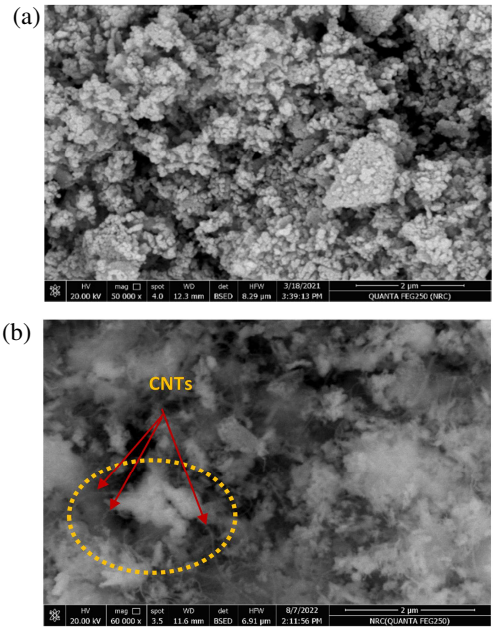

Figure (5: a-b): FE-SEM for $Co_{1.5}Fe_{1.5}O_4$ and CNTs- $Co_{1.5}Fe_{1.5}O_4$ nanocomposites

3.1.6. XPS Analysis

XPS is used to measure the surface properties of non-stoichiometric $Co_{1.5}Fe_{1.5}O_4$, and CNTs/ $Co_{1.5}Fe_{1.5}O_4$ nano-composites. Figures (7: a-g) displays the full-scale C 1s, O 1s, Co 2p, and Fe 2p spectra of these materials.

No other elemental peaks are found, indicating that the CNTs/ $Co_{1.5}Fe_{1.5}O_4$ nano-composite is only made up of C, O, Co, and Fe. Due to spin orbit interactions, the element's 2p state energy level is split into two energy levels, designated 2p3/2 and 2p1/2, respectively. The Co 2p3/2 exhibits two major doublets with peak locations of 779 eV and 781.5 eV

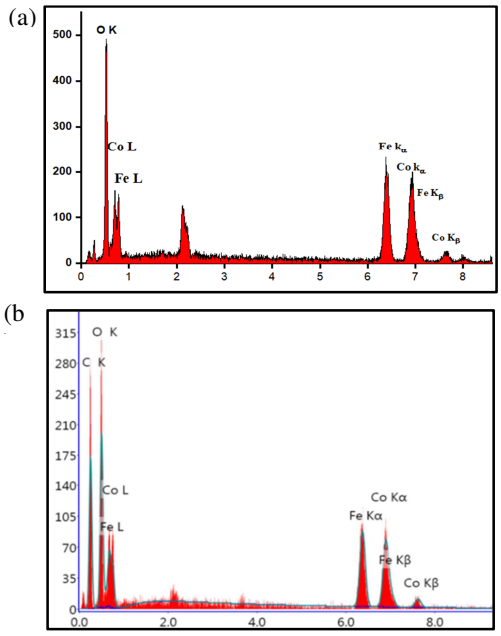

Figure (6: a, b): EDAX spectrum for non-stoichiometric $Co_{1.5}Fe_{1.5}O_4$ and CNTs/$Co_{1.5}Fe_{1.5}O_4$ nano-composite

for the $Co_{1.5}Fe_{1.5}O_4$ sample, and 780 eV and 782 eV for the CNT/ $Co_{1.5}Fe_{1.5}O_4$ nanocomposite sample. These peaks signify the presence of Co2+ ions at the respective B and A sites. While the peak at 787.0 eV is related to its shake-up satellite [38]. Peaks for Co2p1/2 for Co^{2+} are 798.3 eV and 796.0 eV, with an 803.0 eV shake-up satellite speak [39]. Because the Co3+ orbital contains unpaired valence electrons, the low spin Co^{3+} cation produces a weaker satellite peak. [40]. Two main peaks for Fe 2p3/2 and Fe 2p1/2 are obtained for the prepared samples, which correspond to the binding energies of ~710.5 eV and ~724 eV, respectively [41]. Each peak position appears as a doublet peak, indicating the presence of two non-equivalent iron ion bonds and two different types of lattice sites for the occupancy of iron ions [42].

In a non-stoichiometric sample, the O 1s spectrum (Fig. 7: c, g) indicates 2 peaks at 529.51 eV, and 530.99 eV which correspond to metal – O bonds, where metal refers to Co or Fe [43]. The deconvoluted peaks at 530 eV and 531.5 eV, for the CNT/ $Co_{1.5}Fe_{1.5}O_4$ nano-composite are assigned to oxidized groups and metal-O bonds [43]. The obtained data simplify the creation of strong bonding between CNT and $Co_{1.5}Fe_{1.5}O_4$. The composite has broader O 1s peak shapes, than the pure sample, and other peaks corresponding to C 1s Gaussian peaks are observed.

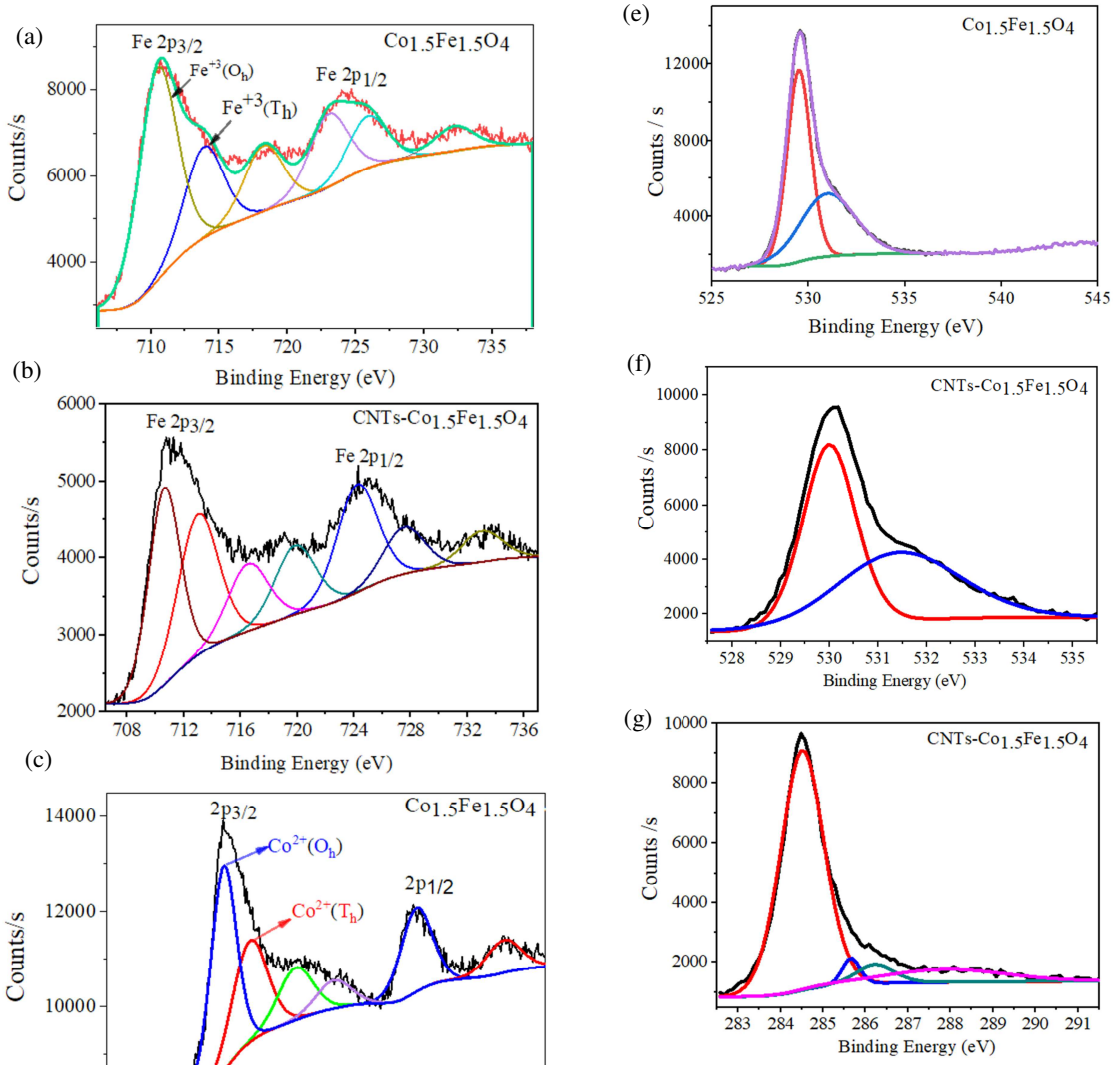

Figure (7: a-g): XPS spectra for (a, b) Fe2p, (c, d) Co2p, (e, f) O1s, and (g) C1s

Figure (7: f) depicts the C 1s spectrum with three peaks. O-C=O groups are attributed to the peak at 286.5 eV, epoxy's C-O at 285.5 eV, and C-C bonding at 284.5 eV [43]. The $Co_{1.5}Fe_{1.5}O_4$ NPs and $Co_{1.5}Fe_{1.5}O_4$/CNTs composite are confirmed by the aforementioned results.

3.1. Magnetic measurements

The magnetic properties of the $Co_{1.5}Fe_{1.5}O_4$ NPs and decorated MWCNTs are examined via the VSM technique. The M-H hysteresis loop of $Co_{1.5}Fe_{1.5}O_4$ and $Co_{1.5}Fe_{1.5}O_4$/CNT are compared with each other as shown in Figure (8: a-c). Various magnetic parameters are determined from the magnetic loops and tabulated in Table (2). Small energy loss and little magnetization are features of the cleared loop.

The Ms has been calculated by analyzing M–H curve at high field using the law of approach to saturation as present in the following equation [44, 45]:

$$M = M_s\left[1 - \frac{a}{H^2}\right] \quad (3)$$

where a is the fitting parameter. By plotting M vs. $1/H^2$, one can approximate the Stoner-Wohlfarth (S-W) theory to notice the values of Ms for $Co_{1.5}Fe_{1.5}O_4$ and $Co_{1.5}Fe_{1.5}O_4$/CNTs [46].

In this manner, the values of M_s can be detected for $Co_{1.5}Fe_{1.5}O_4$ and $Co_{1.5}Fe_{1.5}O_4$/CNTs as 48.14, and 39.44 emu/g, respectively. The fact that the calculated value closely resembles the experimental value suggests that the saturating applied magnetic field of about 20 kOe is suitable for the samples under study.

The experimental magnetic moment (in Bohr's magneton) can be determined from the values of M_s (emu/g) using the formula:

$$n_B = \frac{M\ x\ Ms}{5585} \quad (4)$$

where M is the molecular weight of $Co_{1.5}Fe_{1.5}O_4$. As presented in the table, the CNTs/$Co_{1.5}Fe_{1.5}O_4$ nano-composite exhibits lower magnetic parameters compared to the $Co_{1.5}Fe_{1.5}O_4$ NPs. The investigational nanocomposite's magnetism is reduced by the presence of non-magnetic CNTs, which act as voids when subjected to applied fields and disrupt magnetic circuits. Additionally, the reduction in Ms is possibly due to the non-collinearity of magnetic domains at the surface of $Co_{1.5}Fe_{1.5}O_4$ NPs when attached to CNTs.

The value of the squareness ratio, which ranges from 0 to 1, is a sign of the NPs' softer nature. In the case study, this ratio is smaller than 0.5. According to the S-W model, the $Co_{1.5}Fe_{1.5}O_4$ and CNTs/$Co_{1.5}Fe_{1.5}O_4$ samples interact magneto statically [47]. However, the squareness ratio is influenced by the size of the particles and the fluctuation in anisotropy brought on by an external field. [48].

There is a discernible shift in the loop, which is attributed to exchange bias (H_{EB}) phenomena. The following equation [49] can be used to find the H_{EB}

$$H_{EB} = -\frac{(H_1 + H_2)}{2} \quad (5)$$

This refers to the fact that different spin configurations exist. Additionally, the magnetic structure of the core in a nanostructure sample differs from the surface, where spin frustration is more prominent [50].

Table 2
The saturation magnetization (Ms), remanence magnetization (Mr) , the coercive field (Hc), squareness ratio (Mr/Ms), M-H loop area, magnetic moment (nB), and the exchange bias (EB) for samples

Samples	M_s (emu/g)	M_r (emu/g)	H_C (Oe)	M_r/M_s	Energy loss (erg/g)	n_B exp	EB (Oe)
$Co_{1.5}Fe_{1.5}O_4$	48.14	23.09	1415	0.479	204.69	2.035	0.665
CNTS-$Co_{1.5}Fe_{1.5}O_4$	39.44	19.67	1379	0.498	167.00	1.667	0.400

3.2. Heavy metal removal

The pH solution is considered an important parameter that has a significant impact on the ad-sorption efficiency of the samples [51]. It is crucial in defining several issues, such as ad-sorbent surface charge, degree of ionization, and ad-sorbent interaction [52]. The ad-sorption of Cu^{2+} and Zn^{2+} for the non-stoichiometric $Co_{1.5}Fe_{1.5}O_4$ and CNTs-$Co_{1.5}Fe_{1.5}O_4$ as a function of pH is illustrated in Fig. (9: a-b). The experimental data indicates that the removal efficiency of both Cu^{2+} and Zn^{2+} increases by increasing pH values from 2 to 8 at 30 ^oC. The smallest ion adsorption is observed at low pH (p H = 2). This is explained by the mobility and high concentration of H^+ ions, which favour the ad-sorption of H^+ over Cu^{2+} and Zn^{2+} ions. Consequently, the surface is protonated to form H_3O^+.

To remove Cu^{2+} and Zn^{2+} ions from solutions, more

active adsorbent sites are accessible as a result of a de crease in the amount of protonated species and an inc rease in pH. Electro-static attraction force increases the sorption of metal ions with a +Ve charge, but this can also be clarified by the active sites becoming more neutrally or -Ve charged [53].

According to research by Ali et al. [54], the formation of hydroxyl complexes increases ad-sorption activity at a basic pH of 7. As a result, an increase in the number of metal ions participating in the ad-sorption process has been noticed. The main interactions in the adsorption process are electrostatic, and the obtained data can be elucidated as follows; the hydrolysis products of Fe^{2+} are $FeOH^{+,}$ Fe $(OH)_3^-$, and Fe $(OH)_2$. As the pH increases to 7, these products change. Thus, the surface charge and metal ions have electrostatic forces that are responsible for the adsorption of heavy metal ions. At pH > 8, a balance was achieved between the surface concentrations of Fe $(OH)_3$ and Fe (OH^+), and the efficiency became nearly constant. As a result, pH = 7 is the optimal value for investigating the effect of contact duration on the ad-sorption of Cu^{2+} and Zn^{2+} ions using CNTS-$Co_{1.5}Fe_{1.5}O_4$.

Many authors have investigated the function of carbon nano-tubes in the ad-sorption process. [55]. It has been stated that under identical conditions, the external sites (ES) of MW-CNTs are occupied before the internal sites (IS). As a result, the ES of MW-CNTs is now available for adsorption substances [56]. Furthermore, as discussed by many authors [57-59], CNT caps increase the number of sorption sites and ad-sorption capacity. The p electron density is hydro-phobically assigned to the CNT walls. As a result, the Cu^{2+} & Zn^{2+} will interact hydro-phobically with the MW-CNTs' external wall. In the case of $Co_{1.5}Fe_{1.5}O_4$/ CNTs, the maximum heavy metal removal percent of 100 % and 99.6 % is obtained at pH 7 for Cu, Zn removal respectively. The pattern of heavy metal absorption by functionalized carbon-based nano-materials can be described using the Langmuir-Freundlich, and Temkin isotherm models. The removal of Cu^{2+} and Zn^{2+} metal ions is suggested to be accomplished using the CNTs/$Co_{1.5}Fe_{1.5}O_4$ nano composites as an effective ad-sorbent. Finally, it can be said that CNTs/$Co_{1.5}Fe_{1.5}O_4$ are superior to other ad-sorbents in terms of effectiveness, sustainability, affordability, and environmental impact.

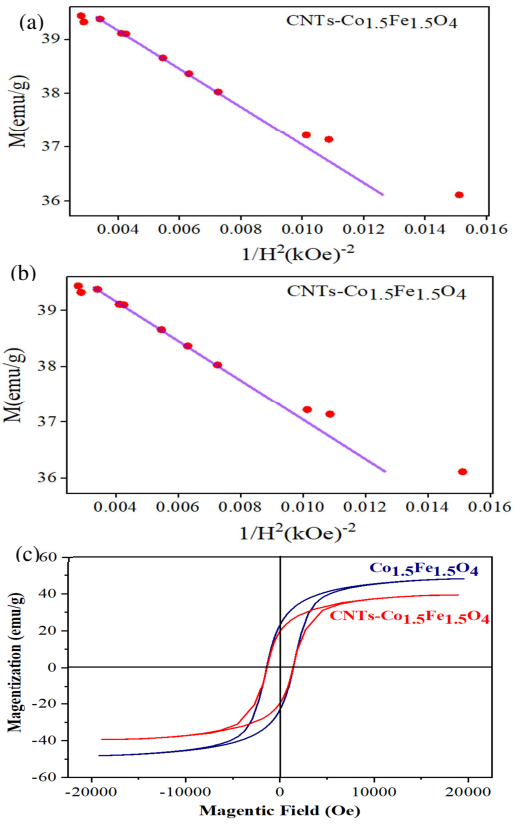

Figure (8: a-c): The hysteresis loops and fitting plot between M versus $1/H^2$ for $Co_{1.5}Fe_{1.5}O_4$ and CNTs-$Co_{1.5}Fe_{1.5}O_4$.

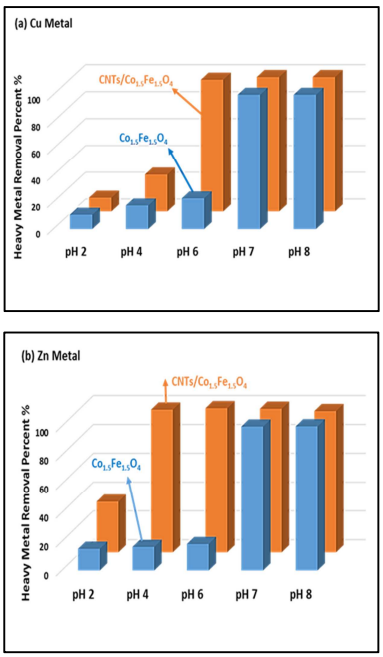

Figure (9: a, b): Effect of pH on $Co_{1.5}Fe_{1.5}O_4$ and CNTs-$Co_{1.5}Fe_{1.5}O_4$ adsorbents for Cu and Zn metal

4. Conclusions

The existence of the intended phases without the detection of any other impurity is evident from the XRD. The observed pattern emphasizes the formation of a cubic spinel structure for the $Co_{1.5}Fe_{1.5}O_4$/CNTs. The polycrystalline structure of the $Co_{1.5}Fe_{1.5}O_4$ composite is revealed by the SAED pattern.

The XPS spectra indicate the presence of Co^{2+} ions in both B and A sites.

The magnetic properties of the investigated nanocomposite are reduced due to the presence of non-magnetic CNTs.

CNTs act as voids when subjected to applied fields and disrupt magnetic circuits.

The CNTs/$Co_{1.5}Fe_{1.5}O_4$ nano-composites can be suggested as a useful ad-sorbent for the removal of Cu^{2+} and Zn^{2+} metal ions.

5. Conflict of interest

There are no conflicts to declare

6. Funding

This research did not receive any specific grant from funding agencies in the public, commercial, or not-for profit sectors.

7. Authors' contribution

Ebtesam E. Ateia contributed to conceptualization, validation, writing–original draft preparation, writing–review & editing, visualization, and supervision.

B. Hussein contributed to material preparation, data curation, and analysis, formal analysis, investigation, optimum selection of material parameters, methodology, validation and visualization, review and editing.

Abdulalah AL-Hamzi: contributed to material preparation, data collection and analysis, formal analysis, investigation, optimum selection of material parameters, methodology, validation and visualization, review and editing.

M. Morsy: preparation carbon nano tubes.

Soha abdelwahab: she was added according to university rules and moral support.

8. Acknowledgements

I would like to express my gratitude and appreciation to Amira. T. Mohamed who has worked actively in the final stage of revising the research.

9. References

1) B. R. Babu, T. Tatarchuk, Mater. Chem. Phys. 207, 534 (2018).
2) L. Bai, M. Pravica, Y. Zhao, C. Park, Y. Meng, S. V. Sinogeikin, and G. Shen, J. Phys. Cond. Matter. 24, 435401 (2012).
3) Xing Ming, Xing Meng, Fang Hu, Chun-Zhong Wang, Zu-Fei Huang, Hou-Gang Fan, and Gang Chen, J. Phys. Condens. Matter. 21, 295902 (2009).
4) A. Kiswandhi, J. S. Brooks, J. Lu, J. Whalen, T. Siegrist, and H. D. Zhou, Phys. Rev. B. 84, 205138 (2011).
5) E. E. Ateia, A.T. Mohamed, M. Morsy, J Mater Sci: Mater Electron.30, 19254–19261 (2019).
6) R. N. Bhowmik, G. Vijayasri, and R. Ranganathan, J. Appl. Phys. 116, 123905 (2014).
7) I. P. Muthuselvan and R. N. Bhowmik, Solid State Sci. 11, 719 (2009).
8) P. Robinson, R. J. Harrison, S. A. MacEnroe, and R. B. Hargraves, Nature. 418, 517 (2002).
9) J. Carrey, B. Mehdaoui, and M. Respaud, J. Appl. Phys. 109, 083921 (2011).
10) M. A. Ateia, E. E. Ateia, M. Mosry, M. M. Arman, Applied Physics A.128,884 (2022).
11) S.-H. Yu and M. Yoshimura, Adv. Funct. Mater. 12, 9 (2002).
12) B. Pan and B. Xing, Environ. Sci. Technol.42, 9005–9013(2008).
13) C. Lu, Y.-L. Chung and K.-F. Chang, Water Res.39, 1183-1189 (2005).
14) M. R. Zakaria, H. Akil, Md, M. H. Abdul Kudus, F. Ullah, F. Javed and N. Nosbi, A Review. Compos. Part B Eng. 176,107313 (2019).
15) M. Morsy, I. S. Yahia, H. Y. Zahran and M. Ibrahim, J. Inorg. Organomet. Polym.29, 416–422 (2019).
16) S. U. Rather, Int. J. Hydrogen. Energy.44,325-331(2019).
17) K. R. Pasupathy and B. Bindu. Microelectronics J.46, 1269–1274 (2015).
18) E. E. Ateia , Amira T. Mohamed , M. Morsy, Metal Oxide-Carbon Hybrid Materials**,** 547-559 (2022), https://doi.org/10.1016/C2019-0-04942-4, Elsevier.
19) Y. Yan, J. Miao, Z. Yang, F. -X. Xiao, H. B. Yang, B. Liu and Y. Yang, Chem. Soc. Rev. 44, 3295-3346 (2015).
20) A. S. Abdulkareem, I. Kariim, M. T. Bankole, J. O. Tijani, T. F. Abodunrin and S. C. Olu. Arab, J. Sci. Eng. 42, 4365–4381(2017).

21) A. Eatemadi, H. Daraee, H. Karimkhanloo, M. Kouhi, N. Zarghami, A. Akbarzadeh, M. Abasi, Y. Hanifehpour and S. W. Joo, Nanoscale Res. Lett.9,1-13 (2014).
22) G. Che, B. B. Lakshmi, C. R. Martin, E. R. Fisher and R. S. Ruoff, Chem. Mater.10, 260–267(1998).
23) E. E. Ateia, A. Al-Hamzi and B. Hussein, J Mater Sci: Mater Electron, 33, 20642 (2022).
24) E. E. Ateia, S. Hussien, A. T. Mohamed, J. Inorg. Organomet. Polym, (2022). https://doi.org/10.1007/s10904-022-02497-5.
25) E. E. Ateia, Mahmoud A. Ateia and M. M. Arman, J. Mater Sci: Mater Electron (2022) 33:8958–8969.
26) N.V. Praskurina, V.A. Cherepanov, O.S. Galynts, V.I. Voronin, Inorg. Mater. 40, 955 (2004).
27) E. E. Ateia, K. Elsayed, D. E. El-Nashar, A Appl. Phys. A. 129, 118 (2023). https://doi.org/10.1007/s00339-023-06388-5 (2023).
28) L. Wang, H. Xing, Z. Liu, Z. Shen, X. Sun and G. Xu. RSC Adv 6:97142e51, (2016).
29) Y. Tang, P. Yin, L. Zhang, J. Wang, X. Feng, K. Wang and J. Dai. Ceram. Int 46:28250e61, (2020).
30) Z. Zhou, Y. Zhang, Z. Wang, W. Wei, W. Tang, J. Shi and R. Xiong, Appl. Surf. Sci. 254, 6972 (2008).
31) E.E. Ateia, G. Abdelatif and F.S. Soliman, J. Mater. Sci: Mater. Electron. 28, 5846 (2017).
32) M. M. Arman and M. A. Ahmed, Appl. Phys. A Mater. Sci. Process. 128, 554 (2022).
33) O. M. Hemeda, A. Tawfik, A. M. A. Henaish and B. I. Salem, Arab J. Nucl. Sci. Appl. 51, 22 (2018).
34) M. W. Smith, I. Dallmeyer, T. J. Johnson, C. S. Brauer, J. McEwen, J. F. Espinal and M.G. Perez, Carbon. 100, 678-692 (2016).
35) J. Fang, T. Liu, Z. Chen, Y. Wang, W. Wei, X. Yue and Z. Jiang. Nanoscale 2016; 8:8899e909.
36) T. Liu, X. Xie, Y. Pang, and S Kobayashi S. J Mater Chem C 2016 ; 4 : 1727e35.
37) R. S. Yadav, J. Havlica, J. Masilko, L. Kalina, J. wasserbayer, M. Hajduchova, V. Enev, I. KuritKa and Z. Kozakova, J. Magn. Magn. Mater. 399, 109–117 (2016).
38) L. Shao, A. Sun, Y. Zhang, L. Yu, N. Suo and Z. Zuo, J. Mater Sci: Mater Electron. 32 20474-20488 (2021).
39) A. Sutka, R. Parna, G. Mezinskis and V. Kisand, Sens. Actuators B Chem. 192, 173–180 (2014).
40) W. P. Wang, H. Hang, T. Xian and J. L. Jiang, Mater. Trans. 53, 1586 (2012).
41) P. Liu, H. He, G. Wei, X. Liang, F. Qi, F. Tan, W. Tan, J. Zhu and R. Zhu, Appl. Catal. B: Environ. 182, 476 (2016).
42) H. Fu, Z.J. Du, W. Zou, H.Q. Li, and C. Zhang, Carbon, 65,112-123 (2013).
43) X. Sun, X. Zhu, X. Yang, J. Sun, Y. Xia, and D. Yang, GEE. 2(2),160-167 (2017).
44) S. Guner, Md. Amir, M. Geleri, M. Sertkol and A. Baykal, Ceram. Int. 41, 10915 (2015).
45) E. E. Ateia, M. K. Abdelamksoud, M. M. Arman, R. Ramadan and A. S. Shafaay, Appl. Phys. A. 125, 516 (2019).
46) Z. L. Wang, Y. Liu and Z. Zhang. Handbook of Nanophase and Nanostructured Materials. Volume III: Materials Systems and Applications I, Kluwer Academic/Plenum Publishers, USA, (2003).
47) R.W. McCallum, J. Magn. Magn. Mater. 292, 135–142 (2005).
48) A. Mumtaz, M. Khan, B. H. Janjua and K. Hasanain, J. Mag. Magn. Mater. 313,266 (2007).
49) A. Enders, R. A. Skomski and J. Honolka, J. Phys. Condens. Matter. 22 (2010) 433001.
50) O.Cador, D.Gatteschi, R.Sessoli, A. Laure, B.Grigore, A.Timco, R. E.P.Winpenny, J. Magn. Magn. Mater. 290–291, Part 1, 55-60 (2005).
51) F. Liu, K. Zhou, Q. Chen, A. Wang and W. Chen. J. Alloys Compd. 773,140 (2019).
52) E.E. Ateia, R. Ramadan and A.S. Shafaay, Appl. Phys. A. 126,222 (2020).
53) I. H. Ali, M. K. Al Mesfer, M. I. Khan, M. Danish and M. M. Alghamdi. Process 2019;7.
54) K. Zare, V. K. Gupta, O. Moradi, A. S. H. Makhlouf, M. Sillanpaa, M. N. Nadagouda, H. Sadegh, R. Shahryari-ghoshekandi, A. Pal, Z. Wang, I. Tyagi and M. Kazemi. M. J Nanostruct Chem 5:227-36, (2015).
55) *H. Mahmoodian*, O. Moradi, B. Shariatzadeha, T. A. Salehf, I. Tyagi, A. Maity, M. Asif and V. K. Gupta. J Mol Liq. 202:189-98, (2015)
56) B. Arora and P. Attri, J. Compos. Sci. 4(3), 135, (2020).
57) DS. Rawat, and M. M. Calbi. J Phys Chem C 111:12980-6(2007).
58) 58) W. Leung Yim , and J. Karl Johnson , J. Chem. Phys. 120, 5377(2004).
59) O. Yahya Bakather, Ain Shams Engineering J. 11(4), 905-912(2020).